A&A 379, 288–304 (2001)
DOI: 10.1051/0004-6361:20011294

Astronomy & Astrophysics

Envelope tomography of long-period variable stars⋆

II. Method

R. Alvarez[1], A. Jorissen[1,⋆⋆], B. Plez[2], D. Gillet[3], A. Fokin[4], and M. Dedecker[1,⋆⋆⋆]

[1] Institut d'Astronomie et d'Astrophysique, Université Libre de Bruxelles, CP 226, Boulevard du Triomphe, 1050 Bruxelles, Belgium
e-mail: ralvarez, ajorisse, dedecker@astro.ulb.ac.be
[2] GRAAL, Université Montpellier II, cc072, 34095 Montpellier Cedex 05, France
e-mail: plez@graal.univ-montp2.fr
[3] Observatoire de Haute-Provence, 04870 Saint-Michel l'Observatoire, France
e-mail: gillet@obs-hp.fr
[4] Institute for Astronomy of the Russia Academy of Sciences, 48 Pjatnitskaja, 109017 Moscow, Russia
e-mail: fokin@inasan.rssi.ru

Received 30 March 2001 / Accepted 11 September 2001

Abstract. A tomographic method is described that makes it possible to follow the propagation of shock waves across the photosphere of long-period variable stars. The method relies on the correlation of the observed spectrum with numerical masks probing layers of different atmospheric depths. The formation depth of spectral lines is derived from synthetic spectra of non-variable red giant stars. When applied to Mira stars around maximum light, the tomographic masks reveal that the deepest photospheric layers are generally characterized by blueshifted absorption lines (attesting to their upward motion), whereas the uppermost layers generally exhibit redshifted absorption lines (indicating their infalling motion). Double absorption lines are found in intermediate layers, where the shock front is located. At later phases, the shock front is seen moving towards upper layers, until it leaves the photosphere.

Key words. stars: AGB and post-AGB – stars: atmospheres – stars: late-type – stars: oscillations – stars: variables: general – shock waves

1. Introduction

Besides the brightness fluctuations, long-period variable stars (LPVs) also exhibit striking spectral changes, like the doubling of several absorption lines around maximum light, first reported by Adams (1941). The line-doubling phenomenon has been a source of conflicting theories. Schwarzschild (1952) has suggested (originally in relation to W Vir Cepheids) that the doubling of the absorption lines around maximum light is related to the passage of a shock wave through the photosphere. Alternative models accounting for line doubling without resorting to differential atmospheric motions have been proposed by Karp (1975) and Gillet et al. (1985).

In Paper I of this series (Alvarez et al. 2000), it was shown that the temporal evolution of the red and blue peaks of the double absorption lines of the Mira variable RT Cyg follows the "Schwarzschild scenario". This result thus indicates that the line-doubling phenomenon is caused by a shock wave propagating in the photosphere. In Paper I, it was shown that this propagation may even be followed by resorting to a tomographic technique. The method relies on the correlation of the observed spectrum with numerical masks probing layers of different atmospheric depths. This technique applied to RT Cyg revealed that the evolution of the line doubling *with atmospheric depth* is also consistent with the Schwarzschild scenario.

This paper presents the implementation of this tomographic technique. Its application to a large sample of LPV stars is presented in Paper III. The possible relationship

Send offprint requests to: A. Jorissen,
e-mail: ajorisse@astro.ulb.ac.be

⋆ Based on observations made at Observatoire de Haute Provence, operated by the Centre National de la Recherche Scientifique, France.

⋆⋆ Research Associate, F.N.R.S. (Belgium).

⋆⋆⋆ F.R.I.A. Research Assistant (Belgium).

between absorption line-doubling and emission lines will be investigated in a forthcoming paper in this series.

2. Scanning different parts of the atmosphere with the default ELODIE correlation masks

Monitoring of a large sample of LPV stars was performed with the fibre-fed echelle spectrograph ELODIE (Baranne et al. 1996) at the Observatoire de Haute-Provence (France). The observations and the star sample are described in detail in Paper III (Tables 1 and 2). The ELODIE spectrograph is designed to perform very accurate radial-velocity measurements by cross-correlating the stellar spectrum with numerical masks. In a first step, the cross-correlation functions (CCF) of the program stars were computed using two different numerical masks included in the ELODIE reduction software: (i) a K0 III mask constructed by Baranne et al. (1996); (ii) a M4 V mask constructed by Delfosse et al. (1999) from an ELODIE spectrum of Barnard's star (Gl 699) applying the method of Baranne et al. (1979).

2.1. Comparison of the CCFs obtained with the K0- and M4-templates

The CCFs obtained for a given LPV star with the K0- and M4-templates are often quite different. Almost all situations may be encountered. The most common are: (i) single peak with similar or different contrasts (Figs. 1 and 2, respectively); (ii) double or asymmetrical peak with both templates (Figs. 3 and 4); (iii) double peak with the K0-template, red peak with the M4-template (Fig. 5); (iv) blue peak with the K0-template, double peak with the M4-template (Fig. 6); (v) doubtful single peak (Fig. 7), doubtful double peak (Fig. 8) or noisy profile (Fig. 9) with the K0-template, single peak with the M4-template.

2.2. Interpretation: A first step towards tomography

The variety of CCF pairs obtained for a given star with the K0- and M4-templates (Sect. 2.1) may be easily explained if one admits that the K0-template probes deeper layers than the M4-template (the validity of this assumption will in fact be demonstrated in Sect. 3.3.2). As may be seen in Fig. 10, the two templates catch different groups of spectral lines. Depending on the phase and on the spectral and chemical types, both, none or only one of the default templates will be able to detect the velocity discontinuity between the deeper, ascending layers and the upper, infalling layers.

It will be shown in Paper III (Table 3 and Sect. 4.3.1) that double peaks are observed more often with the K0-template, whereas the M4-template often reveals only a single red peak (as in Fig. 5). This conclusion is a natural consequence of the fact that (i) the M4-template is more sensitive to the cooler, outermost layers which generally exhibit an infall motion around maximum light (hence the corresponding CCF is a red peak), (ii) the K0-template is more sensitive to hotter, i.e. inner, layers and, hence, is more likely to catch the discontinuity between the ascending and infalling layers (corresponding to a double-peak CCF). A similar conclusion was reached by Hinkle et al. (1984), since the CO $\Delta v = 3$ lines around 1.6 μm, forming deeper in the photosphere than the blue-violet optical lines, exhibit line doubling while the latter do not.

Sometimes however, the M4-template is also able to detect a double peak. In these cases, the K0-template may reveal either a double peak as well, the blue peak being then more pronounced than with the M4-template (Figs. 3 and 4), or solely the blue peak (Fig. 6).

When the star is at minimum light, the discontinuity front has left the photosphere so that the line doubling is no longer visible. The late spectral types exhibited by most LPVs at minimum light prevent us from obtaining a well-defined CCF with the K0-template, which becomes useless. On the contrary, a single-peak CCF can still be obtained with the M4-template (Figs. 8 and 9) which thus delivers a well-defined CCF over the complete light cycle of (oxygen-rich) LPVs.

Another interesting conclusion may be drawn from the comparison of the CCFs obtained with the K0- and M4-templates for stars which exhibit double peaks: the double peak appears at later phases with the M4-template than with the K0-template. As Fig. 11 indicates, a weak secondary peak appears in RT Cyg at phase 0.10 when observed with the M4-template as compared to phase 0.88 with the K0-template. The same conclusion is reached for RY Cep, a Ke-M0e Mira (Fig. 12).

This phase lag can be interpreted once again in terms of the Schwarzschild scenario: since the shock wave propagates outwards and the M4-template scans higher layers than the K0-template, such a phase shift is not surprising. It explains why the doubling is often observed *after* maximum light with the M4-template.

For the same reason, the red peaks observed with the M4-template are almost systematically blue-shifted by 2–4 km s^{-1} compared to the ones observed with the K0-template (see Figs. 4 and 5, and Table 3 of Paper III). This difference may be interpreted in terms of a velocity gradient: since the infalling layers scanned by the M4-template are located above the ones scanned by the K0-template, it seems plausible that these distinct layers fall with different velocities, reflecting the acceleration due to the gravity.

The results discussed in this section thus show that the simultaneous use of the K0- and the M4-templates provides insights into the velocity field of LPV atmospheres. Even more interestingly, the capability of the different templates to probe different layers in the atmosphere, as determined by their different spectral (i.e. temperature) adequacy, provides a hint about how to develop a method to investigate the propagation of the shock wave in LPV atmospheres. This method, which consists of designing specific numerical templates to perform the "tomography" of the atmosphere, is described in detail in Sect. 3.

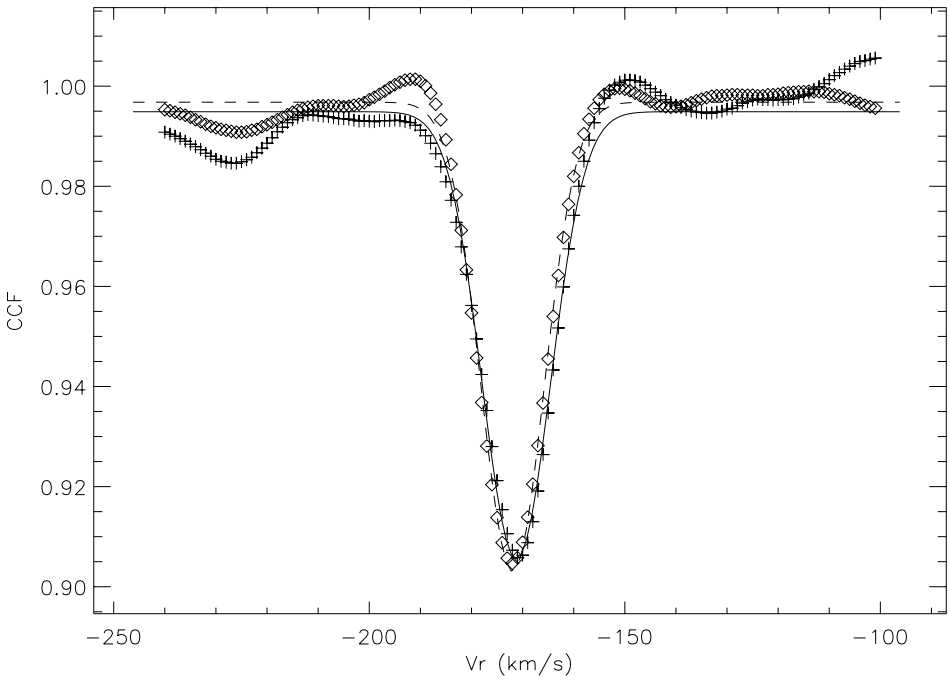

Fig. 1. Cross-correlation profile of V UMi obtained with the default K0 III (crosses) and M4 V (diamonds) masks, during night N7 at phase ∼0.99 (the night number refers to Table 2 of Paper III); the radial velocities as given by gaussian fits are: -171.2 km s^{-1} (K0, solid line) and -171.9 km s^{-1} (M4, dashed line).

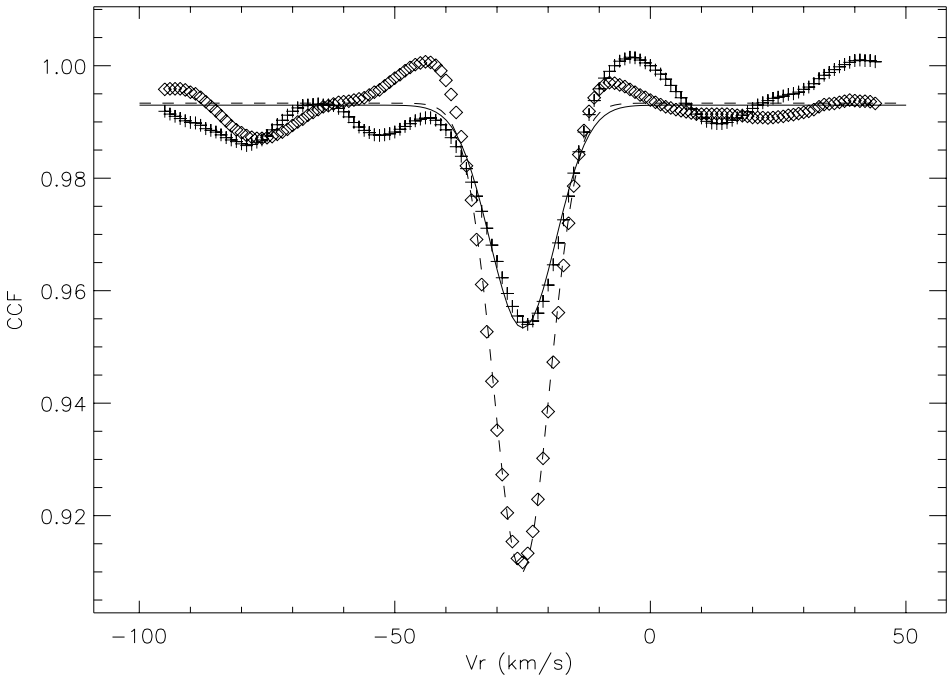

Fig. 2. Same as Fig. 1 for RU Her (night N9, phase 0.02). Radial velocities are: -25.0 km s^{-1} (K0, solid line) and -25.2 km s^{-1} (M4, dashed line).

3. The tomographic technique

The basic idea is to design a set of numerical templates that probe different atmospheric layers, in order to follow the propagation of the shock wave through the atmosphere (a similar technique was applied to BA-type supergiants by Kaufer et al. 1997). This technique takes advantage of the ability of the cross-correlation method to reveal complex profiles despite the severe crowding of the optical spectra. The selective sensitivity of the default K0- and M4-templates demonstrates the potentiality of the method (Sect. 2). The crucial point of the tomographic

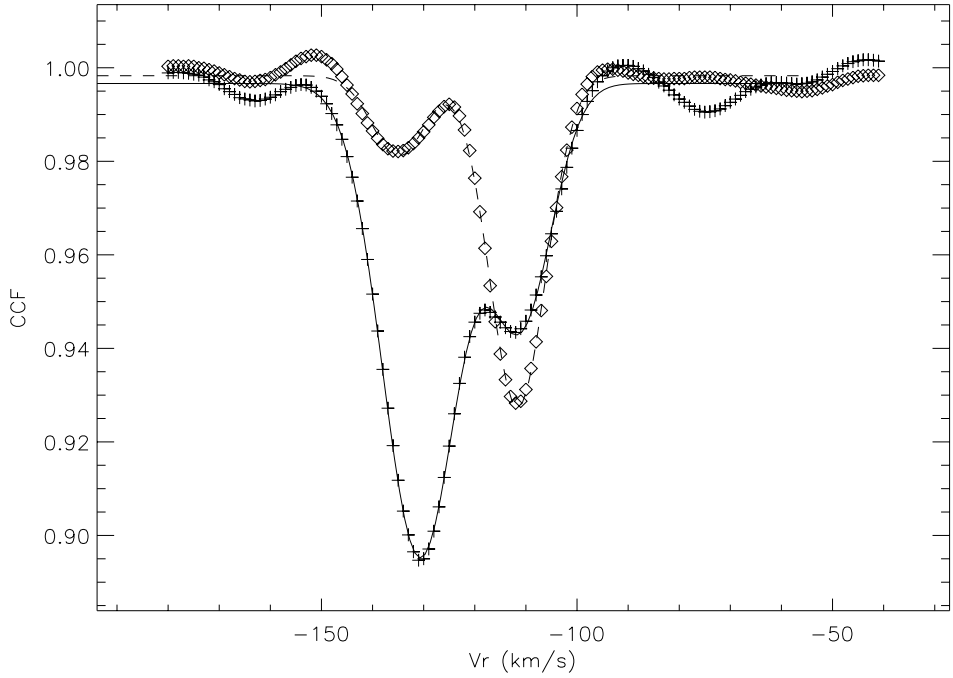

Fig. 3. Same as Fig. 1 for RT Cyg (night N2, phase 1.10). Radial velocities are: $-130.7/-111.0$ km s^{-1} (K0, solid line) and $-134.9/-111.6$ km s^{-1} (M4, dashed line).

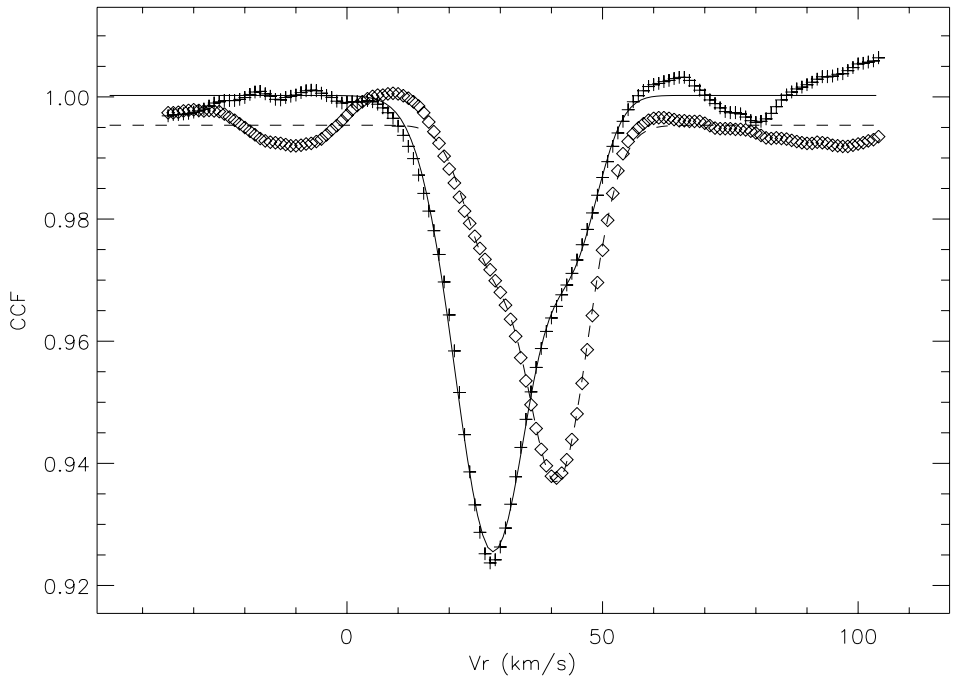

Fig. 4. Same as Fig. 1 for UZ Hya (night N7, phase 1.09). Radial velocities are: $+28.6/+44.8$ km s^{-1} (K0, solid line) and $+27.4/+41.0$ km s^{-1} (M4, dashed line).

technique is the selection of adequate sets of lines forming at a given depth in the atmosphere.

3.1. Synthetic spectra

The tomographic method rests on our ability to construct reliable synthetic spectra of late-type giant stars and to select the right set of spectral lines forming at a given depth. We compute synthetic spectra from static models of red giant stars in spherical symmetry (Plez et al. 1992; Plez 1992) in the spectral range 3850–6900 Å. The synthetic spectra are computed at a high resolution ($\Delta\lambda = 0.03$ Å, which corresponds to the binning step of the ELODIE spectra) using a set of routines

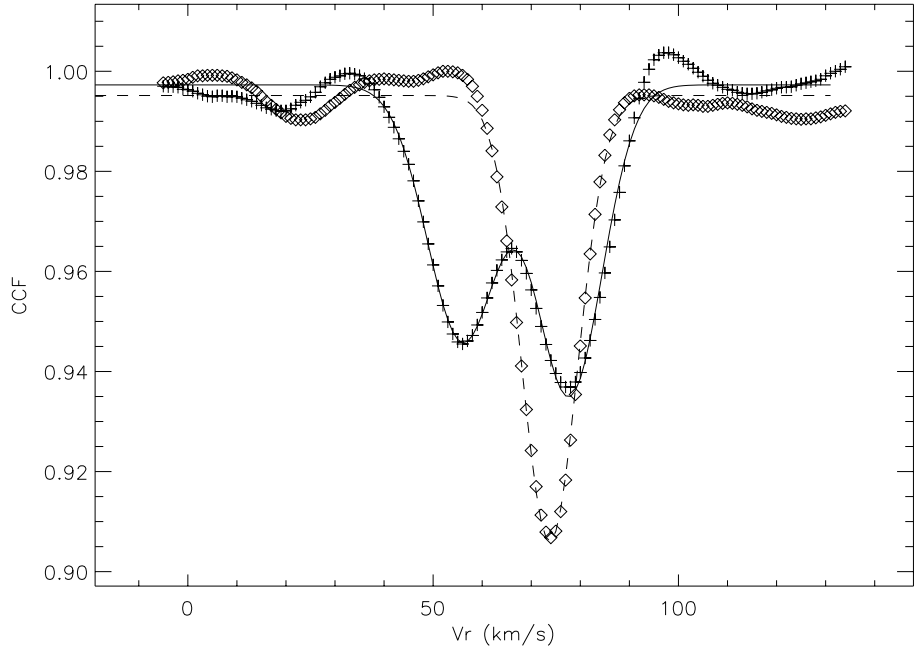

Fig. 5. Same as Fig. 1 for V Tau (night N15, phase 2.01). Radial velocities are: +56.0/+77.8 km s^{-1} (K0, solid line) and +73.8 km s^{-1} (M4, dashed line).

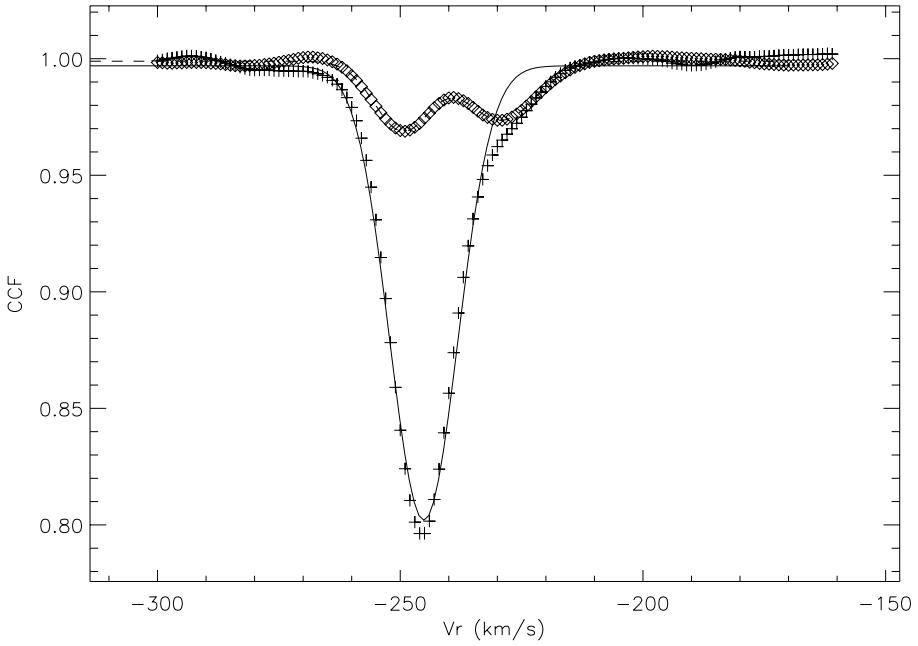

Fig. 6. Same as Fig. 1 for RY Cep (night N4, phase 1.03:). Radial velocities are: −245.1 km s^{-1} (K0, solid line) and −249.5/−229.3 km s^{-1} (M4, dashed line).

especially designed for cool star atmospheric conditions (*Turbospectrum*; see Plez et al. 1993). The spectral synthesis includes the updated line data for TiO (Plez 1998), H_2O and VO as detailed in Bessell et al. (1998) and Alvarez & Plez (1998), plus CH, C_2, CN, NH, OH, MgH, SiH, CaH, ZrO, and atomic lines (Kurucz & Bell 1995). It results in more than 2×10^7 lines. The spectra are computed with CNO abundances and $^{12}C/^{13}C$, $^{14}N/^{15}N$ and $^{16}O/^{18}O$ isotopic ratios (respectively 13, 1250 and 500) typical of red giants (Smith & Lambert 1990).

Figure 13 shows an example of a synthetic spectrum ($T_{\rm eff} = 3500$ K). The dotted line is part of an optical spectrum of HD 123657, an M5-giant, obtained by Serote-Roos et al. (1996) at a resolution of 1.25 Å. The spectral region covered starts at 4800 Å.

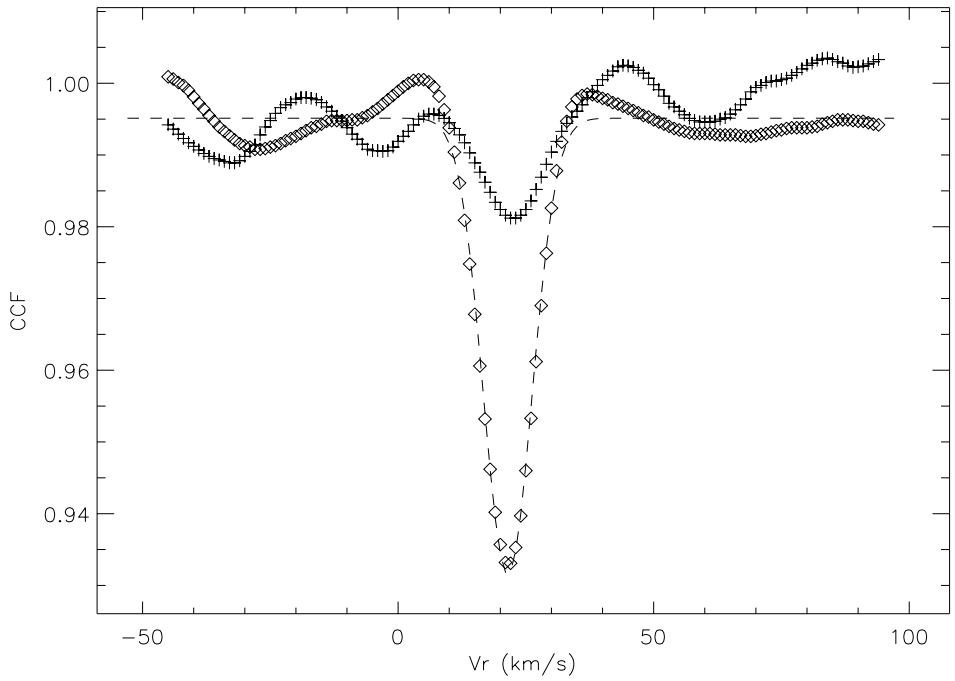

Fig. 7. Same as Fig. 1 for R Peg (night N15, phase 2.00). Radial velocity is: +21.5 km s^{-1} (M4, dashed line).

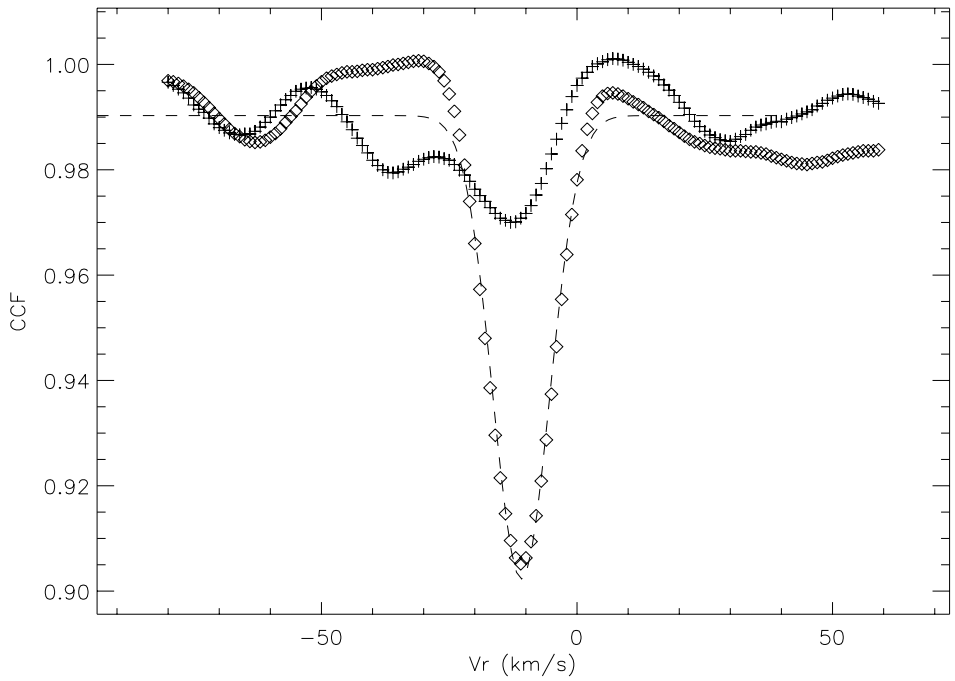

Fig. 8. Same as Fig. 1 for T Cep (night N1, phase 0.23). Radial velocity is: −10.9 km s^{-1} (M4, dashed line).

3.2. Average depth of formation of spectral lines

The static models described in Sect. 3.1 provide us with the monochromatic optical depths τ_λ as a function of geometrical depth, the latter being actually represented in terms of $x = \log \tau_0$, where τ_0 is an optical depth at some reference wavelength (here $\lambda_0 = 1.2$ μm). In static models, the monochromatic optical depth at any reference wavelength is indeed a monotonic function of the geometrical depth in the atmosphere.

In the framework of the Eddington-Barbier approximation, the emergent flux at wavelength λ is supposed to come from the layer with $\tau_\lambda = 2/3$. In the *first implementation* of the tomographic method presented here, we will assume that the line depression forms as well at that same depth. This assumption is valid for sufficiently strong lines, as shown by Magain (1986). Using the expression of

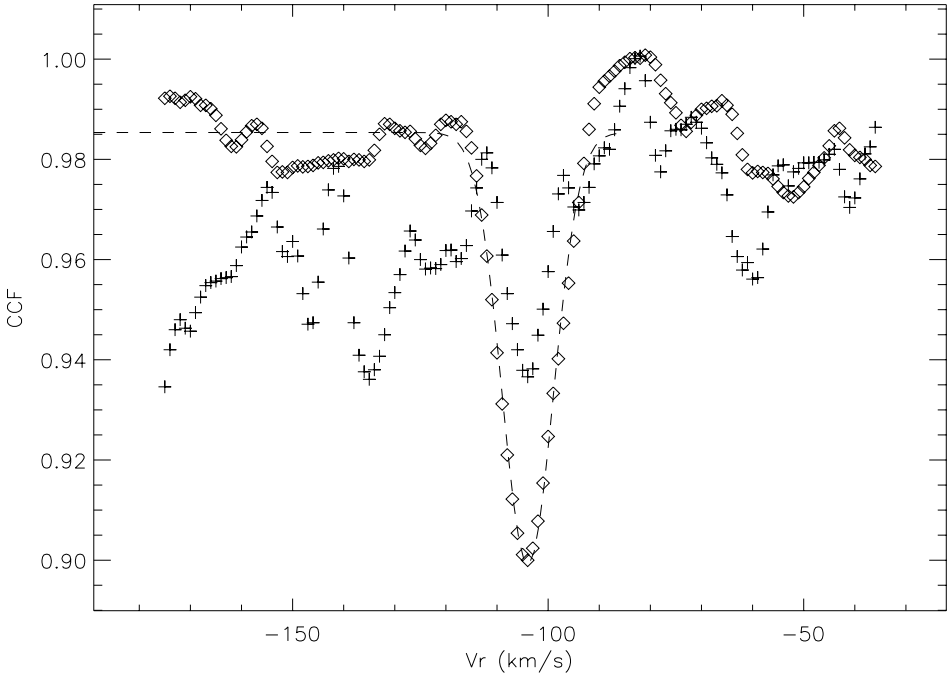

Fig. 9. Same as Fig. 1 for RT Dra (night N12, phase 1.13). Radial velocity is: -104.0 km s^{-1} (M4, dashed line).

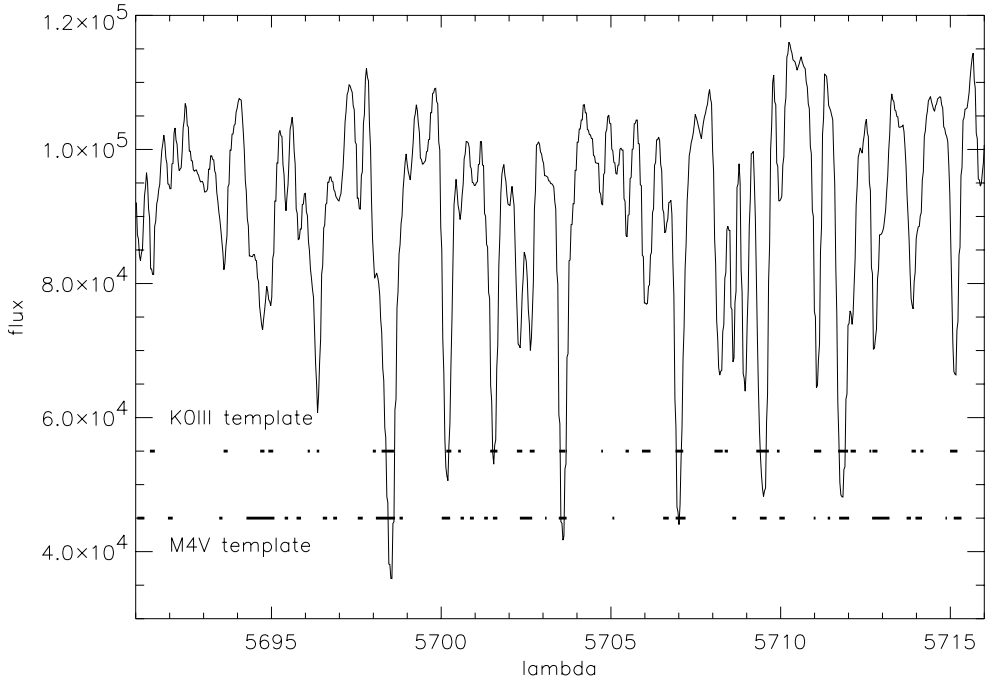

Fig. 10. Part of the spectrum of μ Gem (M3), observed during night N6. The thick segments represent the "holes" of the K0- and M4-templates.

the contribution function (CF)[1] to the line depression in intensity, $C_{\rm R}$, Magain (1986; see also Gurtovenko et al. 1974) has however stressed that the region where the line depression is formed may be different from the region of origin of the emergent intensity, as described by the CF to the line intensity $C_{\rm I}$ (see Albrow & Cottrell 1996 for the generalization to the line depression in flux, in a non-static atmosphere). Magain demonstrates that $C_{\rm R}$ is markedly different from $C_{\rm I}$ in the case of faint lines formed in classical stellar atmospheres (his Fig. 1). In the case of a stronger line $C_{\rm R}$ and $C_{\rm I}$ are more similar, so that the line flux and depression originate in the same layers (his Fig. 2). $C_{\rm R}$ and $C_{\rm I}$ are always close to each other in layers

[1] The contribution function gives the relative contribution of the different atmospheric layers to an observed quantity which can be the emergent intensity or flux or the line depression in the surface intensity or flux.

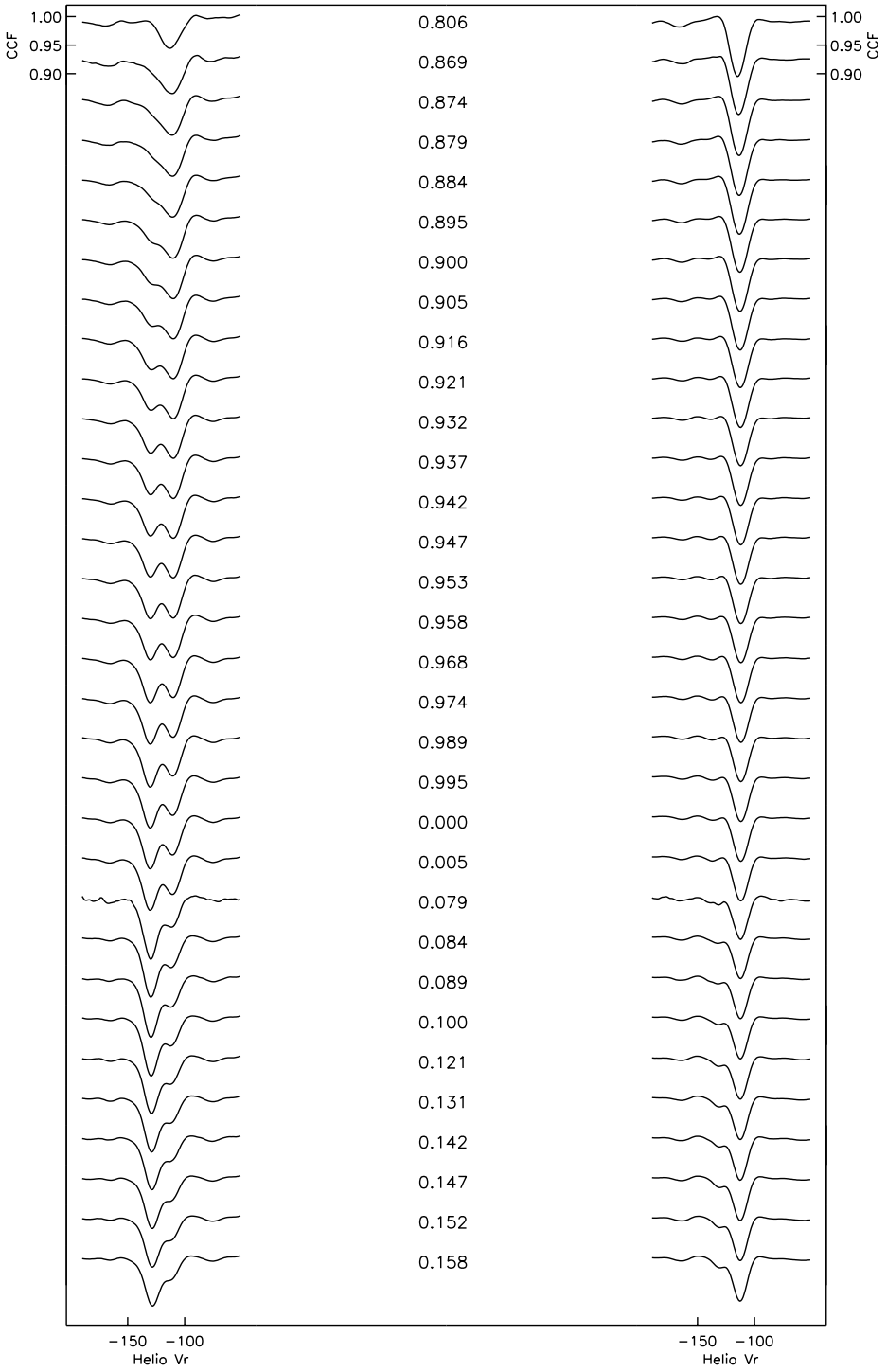

Fig. 11. Sequence of CCFs for RT Cyg obtained with the K0 III mask (left side) and the M4 V mask (right side) during a two-month-long monitoring in August/September 1999. The labels denote the visual phases.

above $\tau_c = 10^{-2}$ (his Fig. 3), i.e. for sufficiently strong lines. Thus masks probing the deepest layers are the more likely to yield poor results, as indicated in Sect. 3.3.2 (see also Fig. 20).

3.3. Designing synthetic numerical templates

The synthetic templates are built in two steps. A complete spectrum, with all atomic and molecular lines included, is computed. The monochromatic optical depth τ_λ is calculated at each depth of the atmospheric model, for each

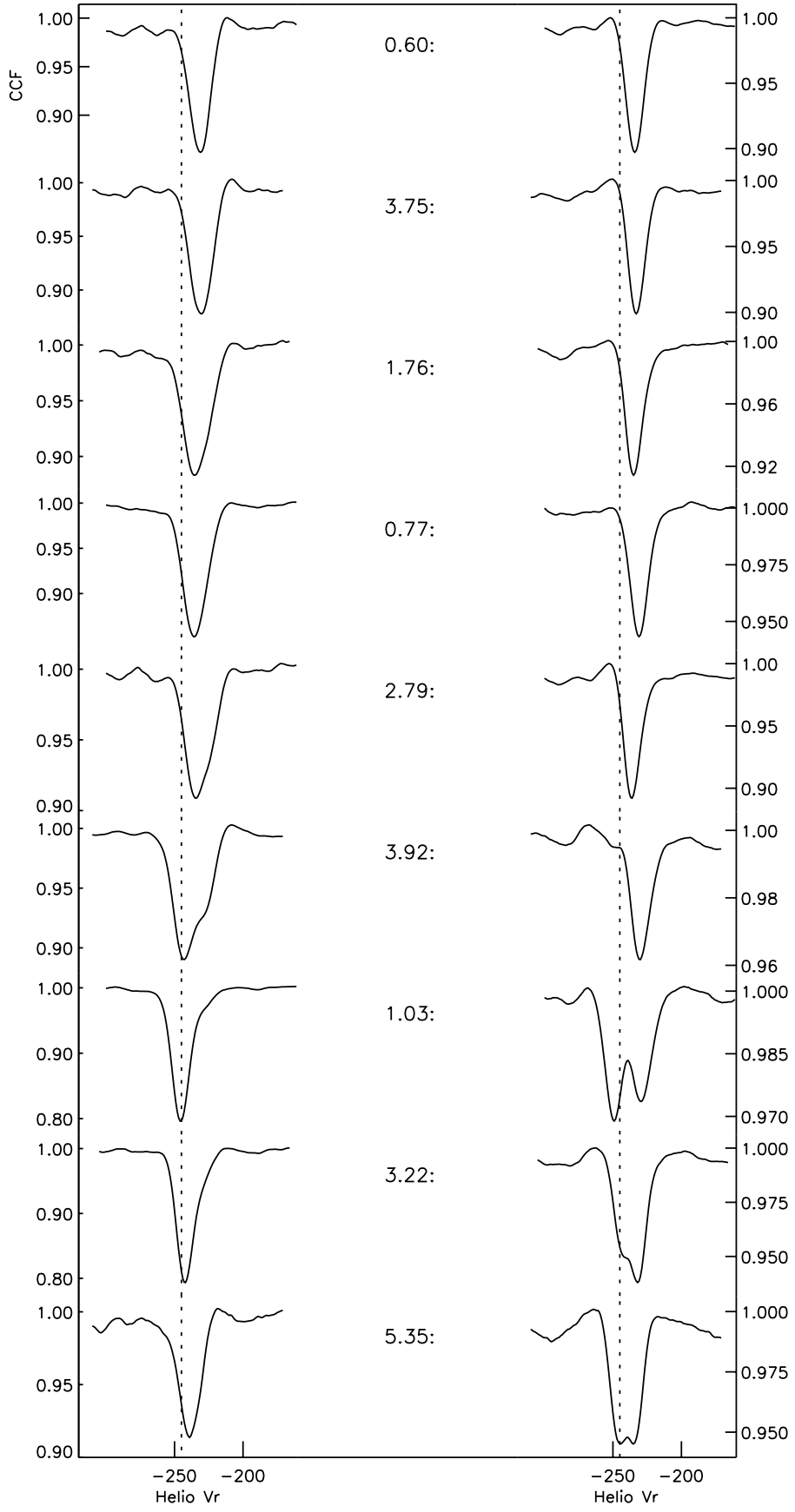

Fig. 12. Sequence of CCFs for RY Cep with the default K0 III mask (left side) and the M4 V mask (right side). The labels denote the visual phases. They are ordered according to increasing fractional phase within each cycle, and are centered around maximum light. The vertical lines are a guide to the eye.

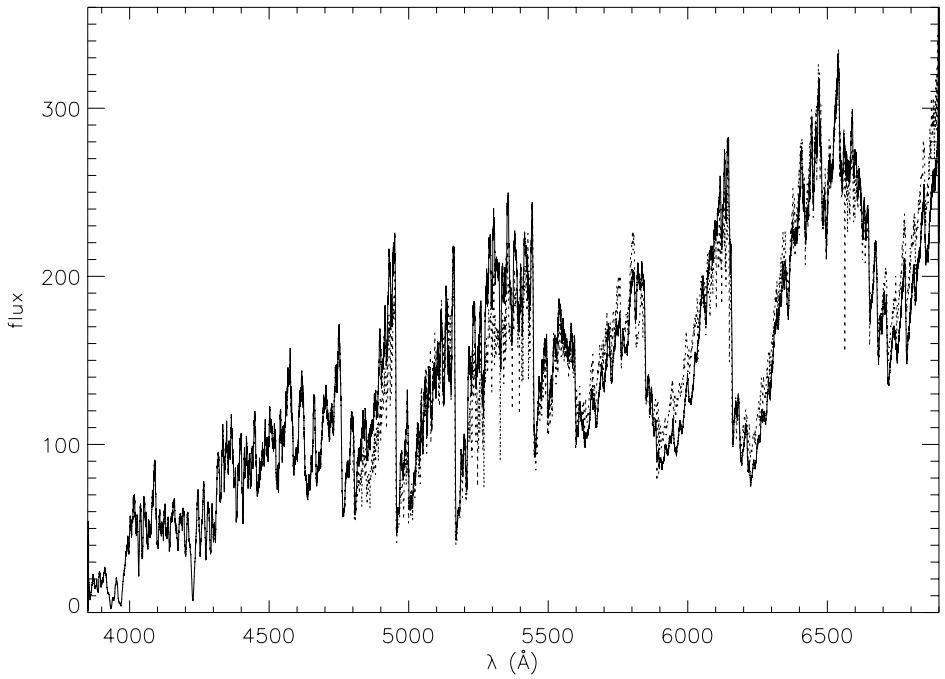

Fig. 13. Synthetic spectrum with $T_{\rm eff} = 3500$ K, $\log g = 0.9$, $M = 1.5\ M_{\odot}$. The dotted line is part of an optical spectrum of HD 123657, an M5-giant, from Serote-Roos et al. (1996).

sampled wavelength. The different masks M_i are then constructed from the collection of N wavelengths $\lambda_{i,j}$ ($1 \leq j \leq N$) such that $x_i \leq x(\tau_{\lambda_{i,j}} = 2/3) < x_{i+1} = x_i + \Delta x$, where $x = \log \tau_0$ is some reference optical depth used to parametrize the geometrical depth. Each mask M_i thus probes lines forming at depths in the range x_i, $x_i + \Delta x$.

Figure 14 illustrates how the synthetic templates are built: for the sake of clarity, only a very small portion (3 Å) of the depth function $x = x(\tau_\lambda = 2/3)$ is represented and the constant Δx has been assigned a very large value ($\Delta x = 2$). The depth function provides the reference optical depth $\tau_0 = 10^x$ – or, equivalently, the geometrical depth – at which the monochromatic optical depth reaches 2/3. The depth function $x = x(\tau_\lambda = 2/3)$ therefore identifies the layer from which the monochromatic flux at wavelength $\lambda_{i,j}$ emerges. The triangles in Fig. 14 denote the local minima of the depth function (they correspond to the spectral lines): when these minima fall in the range scanned by a given template (i.e., between the two horizontal dashed lines), a corresponding "hole" is created in this template (thick dashes at the bottom of the plot).

The constant Δx was chosen after evaluating the contribution function to the emergent flux for some specific atomic lines. It appeared that the typical width $W_{\rm CF}$ of the CFs expressed in the x-scale is about $W_{\rm CF} = 1.5$. The Nyquist-Shannon theorem of elementary signal theory indicates that the optimal sampling of a given function is obtained for $\Delta y/2$ where Δy is the "resolution" of the signal. A value of $\Delta x = W_{\rm CF}/2 = 0.75$ was thus adopted to optimize the thickness of the atmospheric region scanned by each template M_i.

Three sets of numerical templates were built from models with $T_{\rm eff} = 2800$, 3500 and 4250 K. Figure 15 shows the distribution of the depths of line formation for a model with $T_{\rm eff} = 3500$ K: as expected, the number of lines increases with the atmospheric depth (as long as $\log \tau_0 \leq -2$). The lines forming in the outer atmospheric layers are by far less numerous, but they are also more intense. This justifies keeping the same Δx for all masks M_i: the number of lines and their intensities in any given mask vary in opposite directions so as to provide similar signal-to-noise ratios for the CCFs obtained with the different masks (see Figs. 16–18).

When these masks constructed with the complete set of lines were applied to non-variable stars, spurious secondary peaks appeared in the CCFs obtained with some of the masks. These spurious peaks originate in inaccuracies in the wavelengths of some molecular transitions, that are difficult to correct. Therefore, the decision was taken to rely solely on the supposedly more accurate atomic lines for building the templates. A new set of templates M_i' were designed following the method described above, except that they were based on synthetic spectra including only atomic lines. Since important molecular opacity sources are lacking in these synthetic spectra, the associated depth functions may no longer be reliable, casting doubts on the line assignments leading to the new set of masks M_i'.

To circumvent that difficulty, the final masks C_i are constructed by keeping all the holes from the M_i' templates that appeared also in the M_i templates. This guarantees that only the holes associated with atomic lines are kept (as they are present in the M_i' masks),

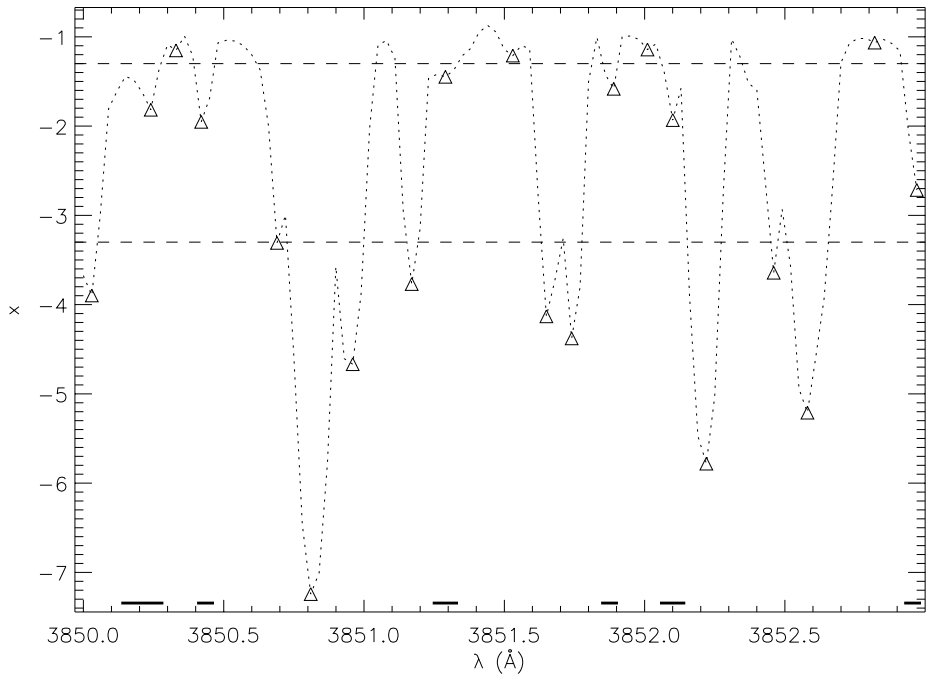

Fig. 14. Illustration of the design of a synthetic template. The present template (thick dashes at the bottom of the plot) scans the lines forming at depths x such that $-1.3 \leq x < -3.3$ (see text).

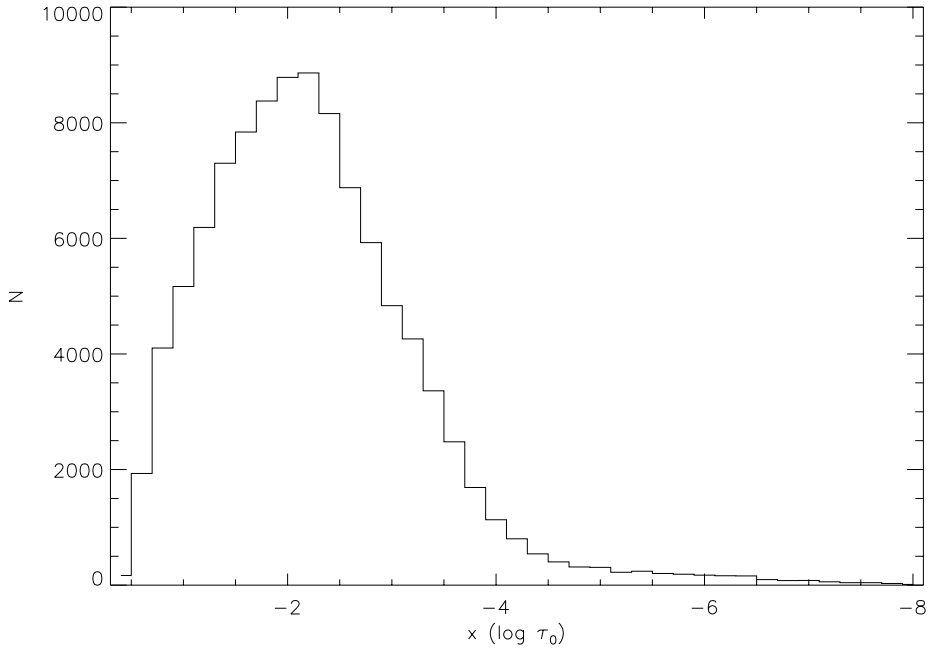

Fig. 15. Number of lines as a function of their formation depth (expressed in the log τ_0 scale, where $\lambda_0 = 1.2$ μm) for a model at $T_{\rm eff}$ = 3500 K.

and that they are located in the right template, i.e. the template which scans the right depth range $[x_i,\, x_i + \Delta x]$ (as they are also present in the M_i masks). This two-step procedure has the advantage of being easy to manage and avoids the enormous task of directly identifying which line (among the millions) contributes to a given hole before deciding to keep it or not. Table 1 gives for each atmospheric model the total range of reference optical depths x scanned by the masks, the depth step Δx and the number of lines per mask C_i. The masks C_i are available at `http://www-astro.ulb.ac.be/Html/home.html#tomography`.

At this point, a comment should be made about the validity of the use of *static* models to design templates to be used on dynamical atmospheres. Let us first remark

Table 1. The synthetic templates.

Model ($T_{\rm eff}$, $\log g$)	2800 K, −0.4	3500 K, 0.9	4250 K, −0.5
Total range scanned (x-scale)	$-2.75 \rightarrow -6.50$	$-2.00 \rightarrow -8.00$	$-1.50 \rightarrow -7.50$
Δx	0.75	0.75	0.75
Masks		# of lines per mask	
C_1 (innermost)	211	777	1337
C_2	186	610	1099
C_3	193	433	873
C_4	160	321	602
C_5	99	168	323
C_6	—	167	184
C_7	—	94	124
C_8 (outermost)	—	46	47

that, if one aims at uncovering the complex line profiles of LPVs caused by the dynamics of their envelope, the correlation of the observed spectrum with a mask constructed from a dynamical model is not the way to go. In the ideal case where the dynamical model used to construct the template would perfectly match the real star, the resulting CCF would be very sharp and single-peaked. To reveal the various velocities characterizing the different layers moving in the envelope, one needs to start instead from templates constructed from static models!

The real difficulty in the application of "static" templates to dynamical atmospheres is elsewhere. It is clear that the contribution function to the line depression (Sect. 3.2) may acquire several local maxima in a dynamical atmosphere (see e.g., Albrow & Cottrell 1996). This is precisely why the line shape acquires complex profiles in dynamical atmospheres, which simply reflect the complex shape of the contribution function. The condition that needs to be satisfied for the tomographic method to yield reliable results with "static" masks is the following: the contribution functions of *all* the lines that were assigned to a given static mask should change in the *same* way when passing from a static to a dynamic atmosphere. In other words, the lines supposed to form in the same layers in a static atmosphere should still form in the same (possibly becoming non connected) layers in a dynamical atmosphere. Or equivalently, there should be no swapping of lines between masks when passing from a static to a dynamic atmosphere. We defer to a forthcoming paper the test of how well this assumption is satisfied in practice. At this stage, we can only provide empirical, a posteriori evidence that this condition does not seem to be very badly violated. This empirical evidence relies on the fact that (i) the CCF shapes vary gently and smoothly from one mask to the next (see Figs. 17 and 18), and (ii) the evolution of the CCF shape from one mask to the next reflects what is expected in the framework of the Schwarzschild scenario (see Fig. 4 of Paper I).

A further confirmation of the validity of our method is provided a posteriori by the discussion of Sect. 3.3.3, which shows that the CCF correctly reproduces the complex shapes observed in a dynamical atmosphere for the lines probed by the considered mask (see Fig. 21).

3.3.1. Application to non-variable stars

In order to check whether our synthetic templates are reliable, the CCFs of the non-variable stars of the sample have been computed with the newly designed masks. The sequence of CCFs obtained for μ Gem, a M3 giant, with the 3500 K templates is presented in Fig. 16. The CCFs obtained with the K0- and M4-templates are also displayed for comparison.

It can be seen that the synthetic masks C_i yield the same radial velocity to within 0.45 km s^{-1} rms (excluding the mask C8 which delivers a very broad CCF). Figure 16 also shows that the contrast of the CCFs increases along the sequence C_1 to C_8. This is not surprising since, from C_1 to C_8, each template scans stronger and stronger lines (i.e. forming closer and closer to the surface), and the CCF contrast reflects the average intensity of the group of lines scanned. It is also remarkable to note that the "signal-to-noise" ratio of the CCFs (ratio of the fluctuations of the continuum level to the depth of the peak) remains more or less constant. Also note how the wings of the CCF strengthen from C_1 to C_8, revealing a similar – and expected – change in the profiles of the lines scanned.

3.3.2. Application to variable stars

Now that the reliability of the synthetic masks has been assessed from their application to non-variable stars (Sect. 3.3.1), they may be applied to variable stars. Figures 17 and 18 present the sequence of CCFs obtained with the synthetic templates of the $T_{\rm eff}$ = 3500 K series for Z Oph and V Tau during night N1 (phase 0.08) and N4 (phase 0.08) respectively; they clearly reveal a transition from a single blue peak (templates C_1–C_3) to a red one (C_8) through double profiles (C_4–C_7). Again, the Schwarzschild scenario reveals itself, but this time in a *spatial* rather than *temporal* sequence. The deeper the mask

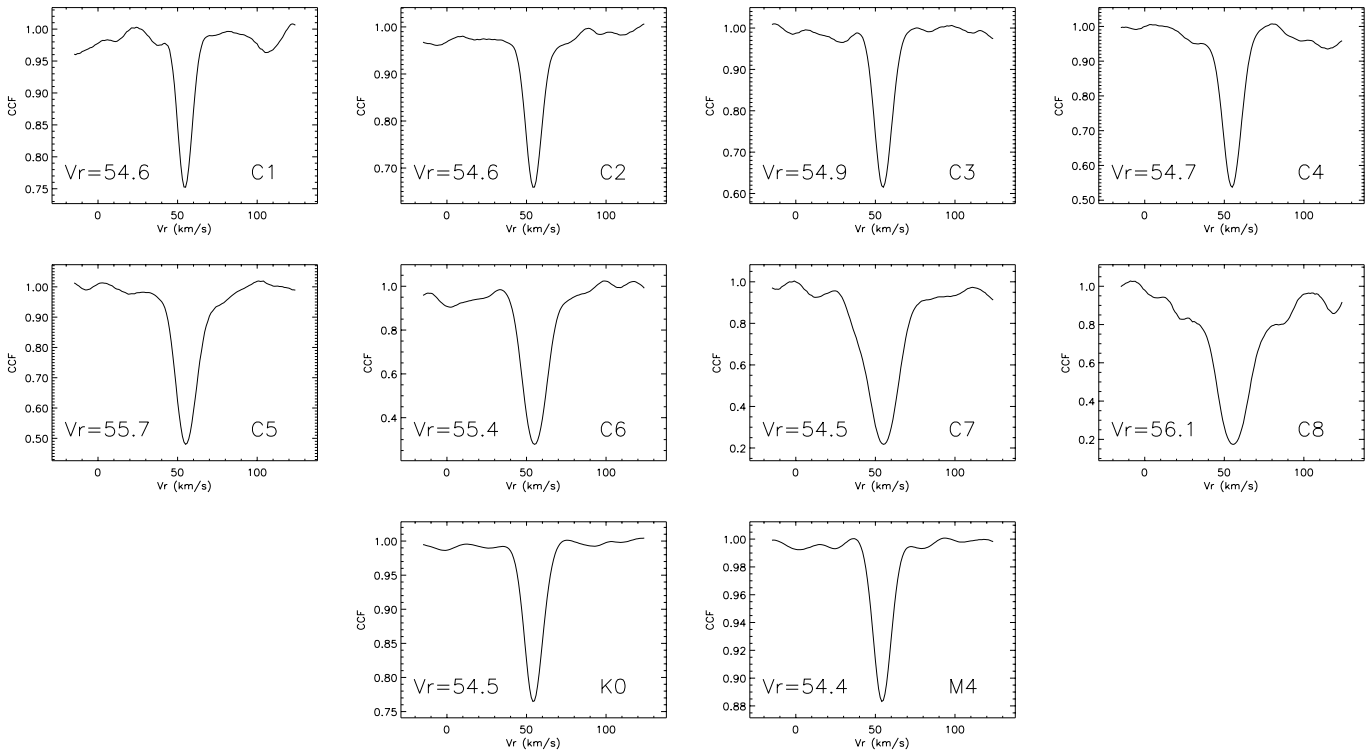

Fig. 16. Sequence of CCFs obtained for μ Gem with the synthetic templates of the $T_{\rm eff}$ = 3500 K series. Labels refer to the template names (see Table 1). The sequence goes from the innermost (top left) to the outermost (bottom right) layers. The CCFs obtained with the K0- and the M4-templates are also displayed. Note how the CCF wings and contrast increase from C_1 to C_8.

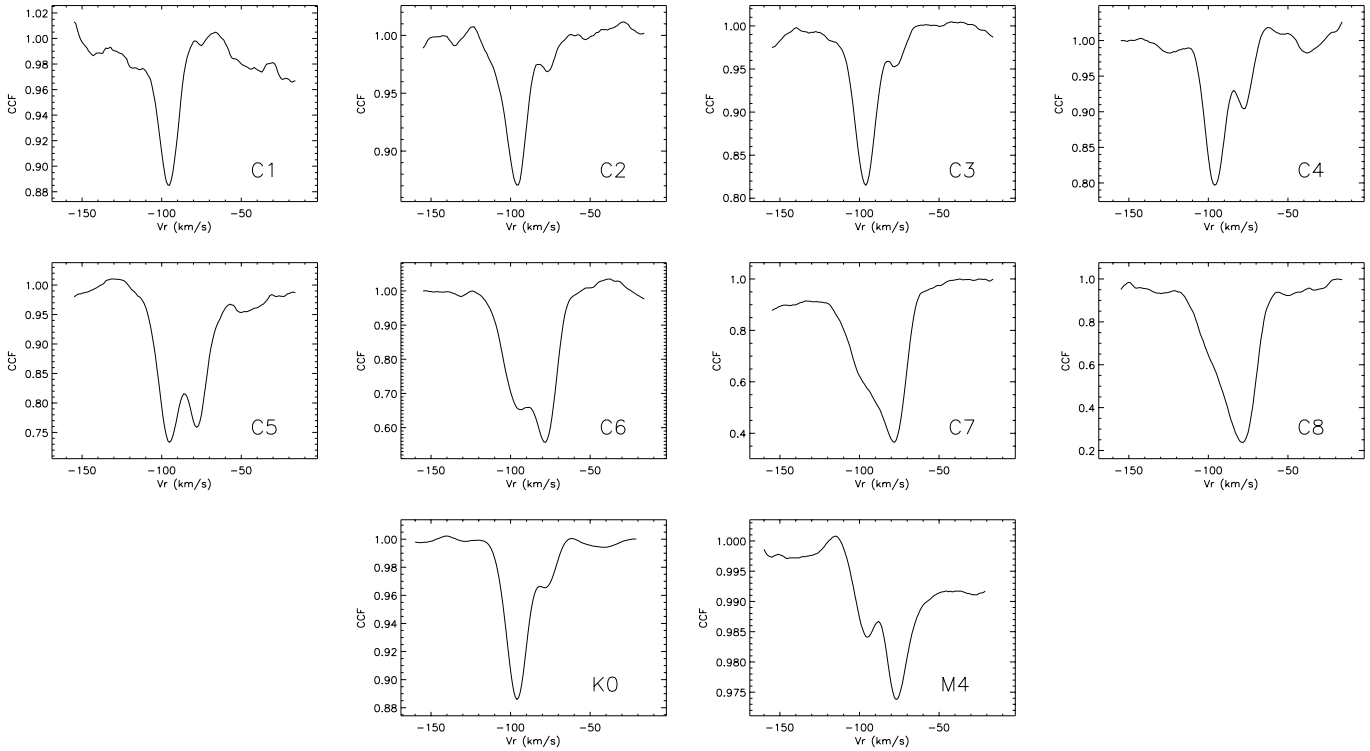

Fig. 17. Sequence of CCFs obtained for Z Oph (night N1, phase 0.08) with the synthetic templates of the $T_{\rm eff}$ = 3500 K series. Labels have the same meaning as in Fig. 16.

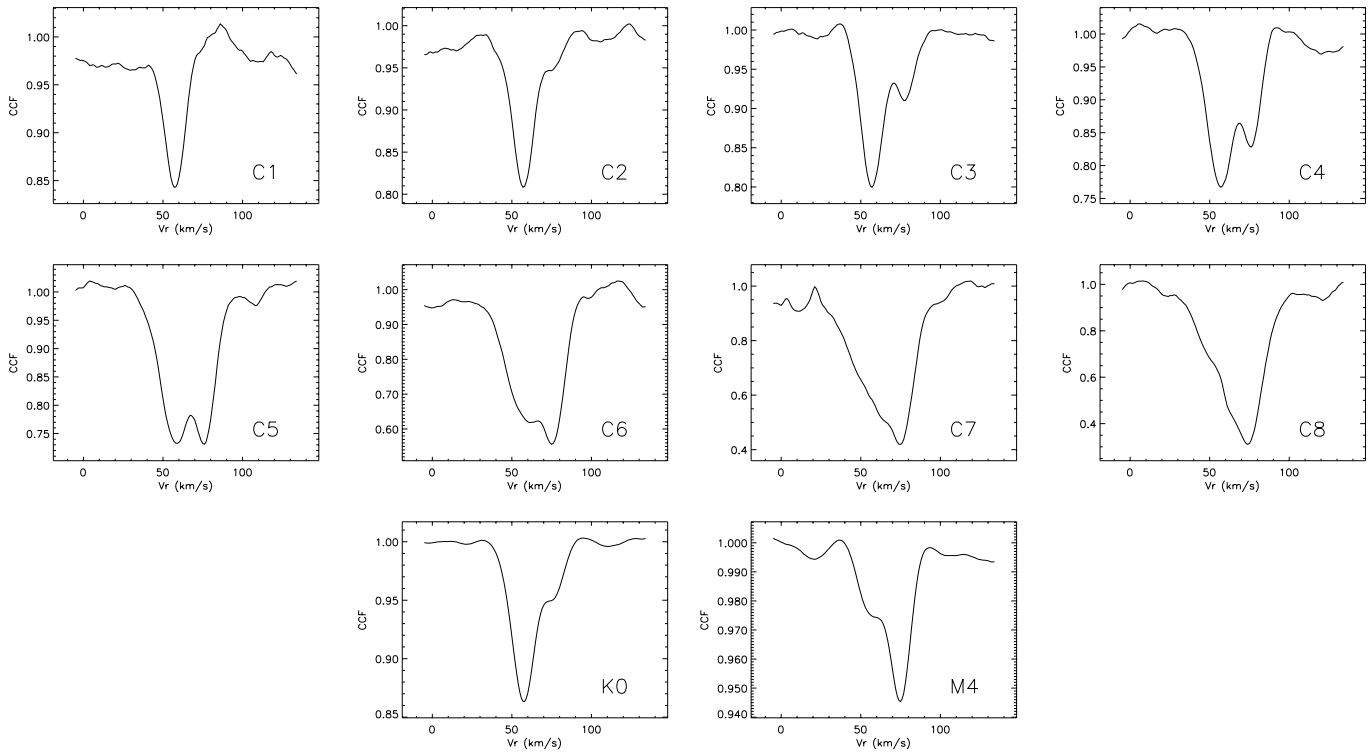

Fig. 18. Sequence of CCFs obtained for V Tau (night N4, phase 0.08) with the synthetic templates of the $T_{\rm eff}$ = 3500 K series. Labels have the same meaning as in Fig. 16.

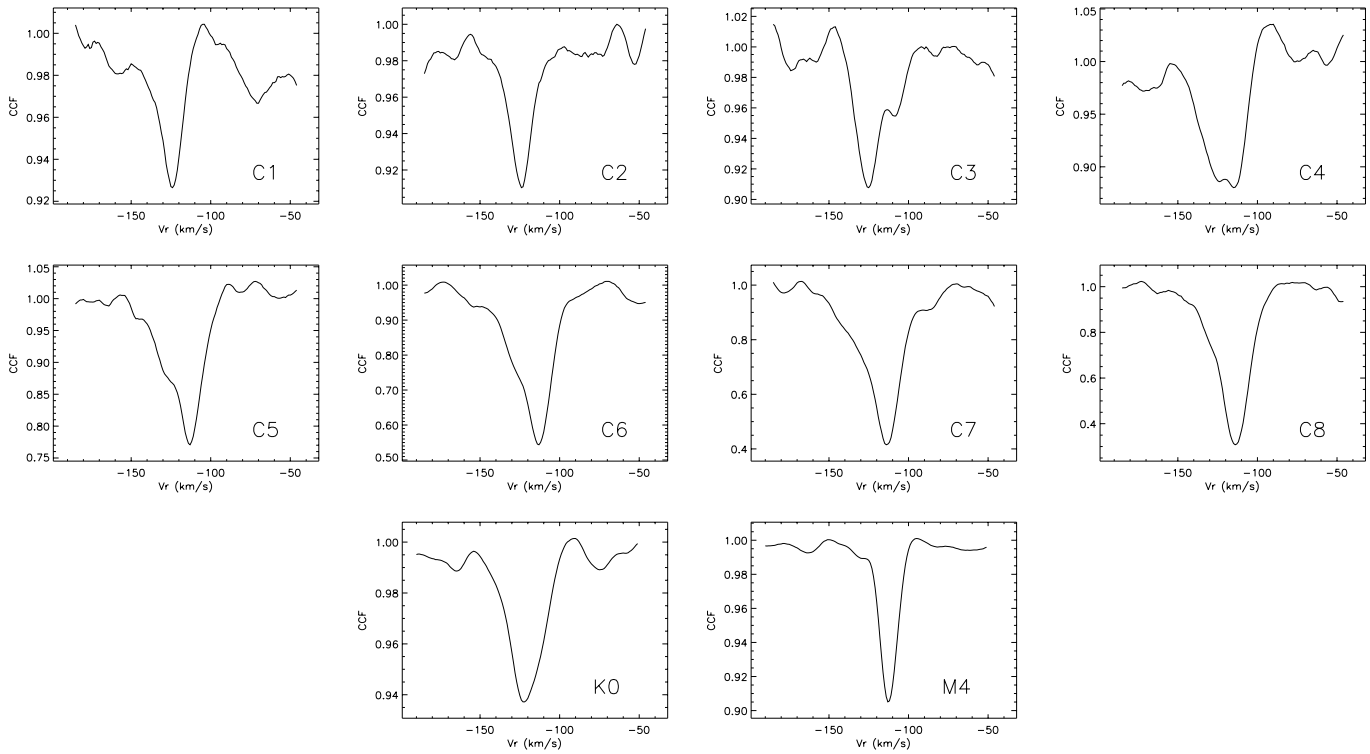

Fig. 19. Sequence of CCFs obtained for RT Cyg (night N3, phase 1.23) with the synthetic templates of the $T_{\rm eff}$ = 3500 K series. Labels have the same meaning as in Fig. 16.

scans, the more intense the blue peak is (and conversely for the red peak). With the synthetic templates, it is thus possible to follow the change of the CCFs from one layer to the next, i.e. to monitor the velocity field across the atmosphere.

It is also interesting to note that the CCF obtained with the C_2-template (i.e. deep layers) is very similar to the one obtained with the K0-template, whereas the C_6- and C_7-templates (outermost layers) give profiles similar to those obtained with the M4-template. This similarity corroborates the conclusion of Sect. 2 on the different depths probed by the two default K0- and M4-templates.

Figure 19 provides another illustration of the efficiency of the synthetic templates: while each of the default templates yields a single peak (although rather asymmetrical for the K0-template) for RT Cyg at phase 1.23, the C_3- and C_4-templates clearly reveal that line-doubling is actually present in that star for the specific set of lines probed by the masks C_3 and C_4. We refer the reader to Paper I for the application of the tomographic masks to a sequence of spectra of RT Cyg covering phases 0.81 to 1.16, which clearly reveals the outward propagation of the shock front.

The tomographic masks yield somewhat poorer results for late-type LPVs. As an illustration, Fig. 20 shows the application of the tomographic masks to the late-type LPV RU Her (M6-M9). Like the M4V mask, the outer masks C4 to C8 (of the 3500 K set) yield a well-contrasted, but sometimes quite asymmetric, CCF. The innermost masks C1 and C2 provide a CCF that is, however, totally useless. The C3 mask presents several secondary peaks (that are reminiscent of those obtained with the K0III template). The peak at $V \sim -50$ km s^{-1} remains visible in the C4 and C5 CCFs, but it is difficult to assess whether it traces a real layer or whether it must be ascribed to some kind of "correlation noise" due to the mismatch between the template and the observed spectrum. A future implementation of the tomographic method (lifting some of the simplifying hypotheses described in Sect. 3) should hopefully improve the results for late-type LPVs.

3.3.3. Individual lines and cross-correlation profiles

A definite proof that the complex CCF profiles of LPVs as observed for instance in Figs. 17 or 18 are not an artefact of the method, is provided by the comparison of the CCF profile with the shapes of individual lines probed by the corresponding mask. For this purpose, an early-type LPV must be selected, to avoid too severe spectral crowding. Z Oph (K3 at maximum) has the earliest spectral type in the sample. Figure 21 compares the λ 6358.69 Fe line at 4 different phases (bottom row) with the CCFs obtained with the K0-, M4- and C_5-templates (from top to bottom), since the λ 6358.69 line belongs to the C_5-template. The CCFs obtained with this template (third row) reproduce remarkably well the shape of the λ 6358.69 line. On the contrary, the shapes of the CCFs obtained with the K0- and M4-templates are noticeably different, since they were shown to correspond instead to the C_2 and C_6–C_7 templates respectively (Sect. 3.3.2). This is clear evidence that the CCFs obtained with the synthetic templates correctly reflect the shape of the set of lines they scan (at least in the case of early-type LPVs). This result may be seen as an a posteriori validation of the tomographic method as a whole (at least for early-type LPVs; see Sect. 3.3.2 and Fig. 20 for a discussion of late-type LPVs) and of the various assumptions involved (use of "static" masks, Eddington-Barbier approximation for the depth of formation of spectral lines...) as discussed in Sect. 3.

3.3.4. Comparison of CCFs obtained with synthetic templates constructed from models of different temperatures

This section briefly addresses the question of the influence of the model used to construct the synthetic templates on the resulting CCFs of LPVs. Browsing the large database containing the CCFs computed with the tomographic masks of the $T_{\rm eff}$ = 4250, 3500 and 2800 K series for all 315 available LPV spectra (Table 3 of Paper III) has shown that (i) the masks based on the 4250 K and 3500 K series are the most appropriate to perform the tomography of LPVs (since the CCFs obtained with masks C_1, C_2 of the 2800 K series are generally noisy[2] – see also Fig. 20 in Sect. 3.3.2); (ii) no information that is not already present in the CCFs of the 4250 K series is obtained with the CCFs from the other two series. Schematically, the CCFs of the three series match each other after translating one sequence with respect to the other, i.e., the CCF of template C_i(4250 K) is almost identical to the CCF of template C_{i-1}(3500 K).

4. Summary

A tomographic method has been described that makes it possible to follow the propagation of the shock wave across the photosphere of LPV stars. The method relies on the correlation of the observed spectrum with numerical masks probing layers of different atmospheric depths. The tomographic masks are constructed from synthetic spectra of red giant stars that provide the depth of formation of spectral lines. When applied to Mira stars around maximum light, they reveal that the deeper layers are generally characterized by blueshifted absorption lines (translating their upward motion), whereas the uppermost layers generally exhibit redshifted absorption lines (translating their infalling motion). A double-peak profile is then found in intermediate layers, where the shock front is located. At later phases, the shock front is seen moving towards upper layers, until it leaves the photosphere.

[2] Note that this poor result may be due to the condition $\tau_\lambda = 2/3$ used to define the depth of formation of the line depression, which was shown in Sect. 3.2 to be poorly satisfied in the case of faint lines.

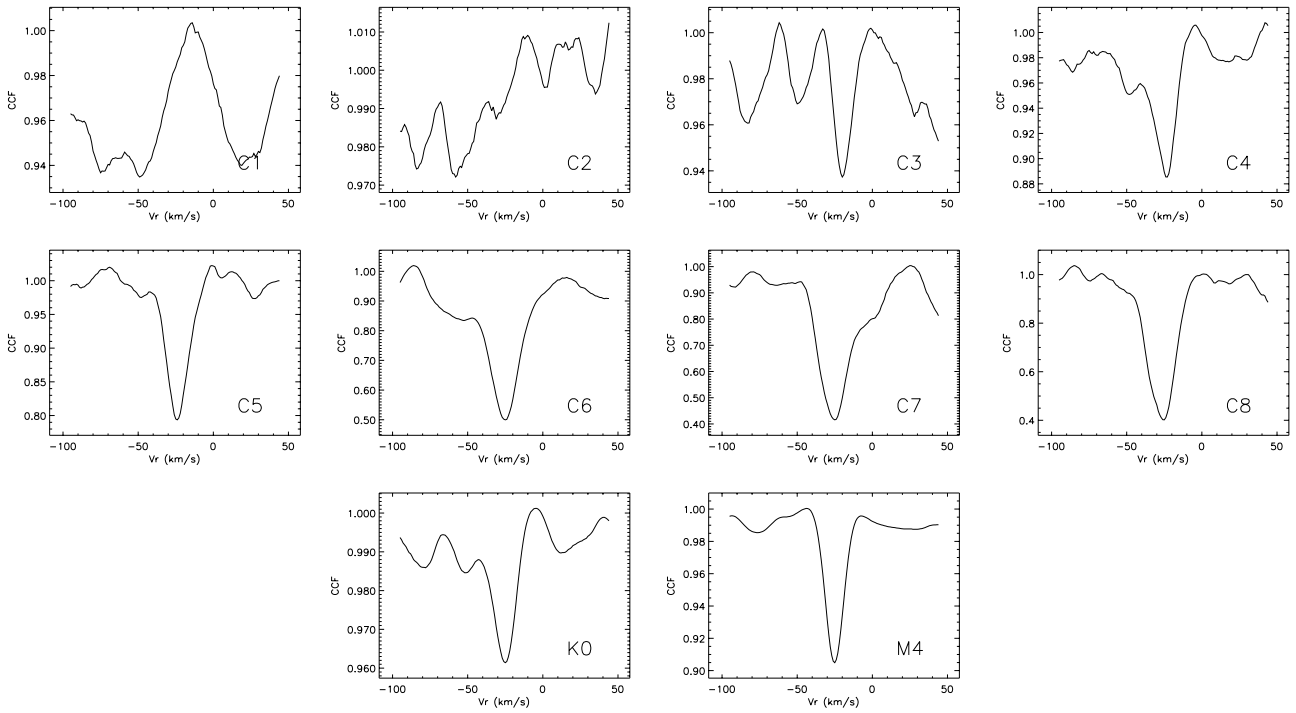

Fig. 20. Sequence of CCFs obtained for the late-type LPV RU Her (M6-M9; night N10, phase 0.08) with the synthetic templates of the $T_{\rm eff}$ = 3500 K series. Labels have the same meaning as in Fig. 16.

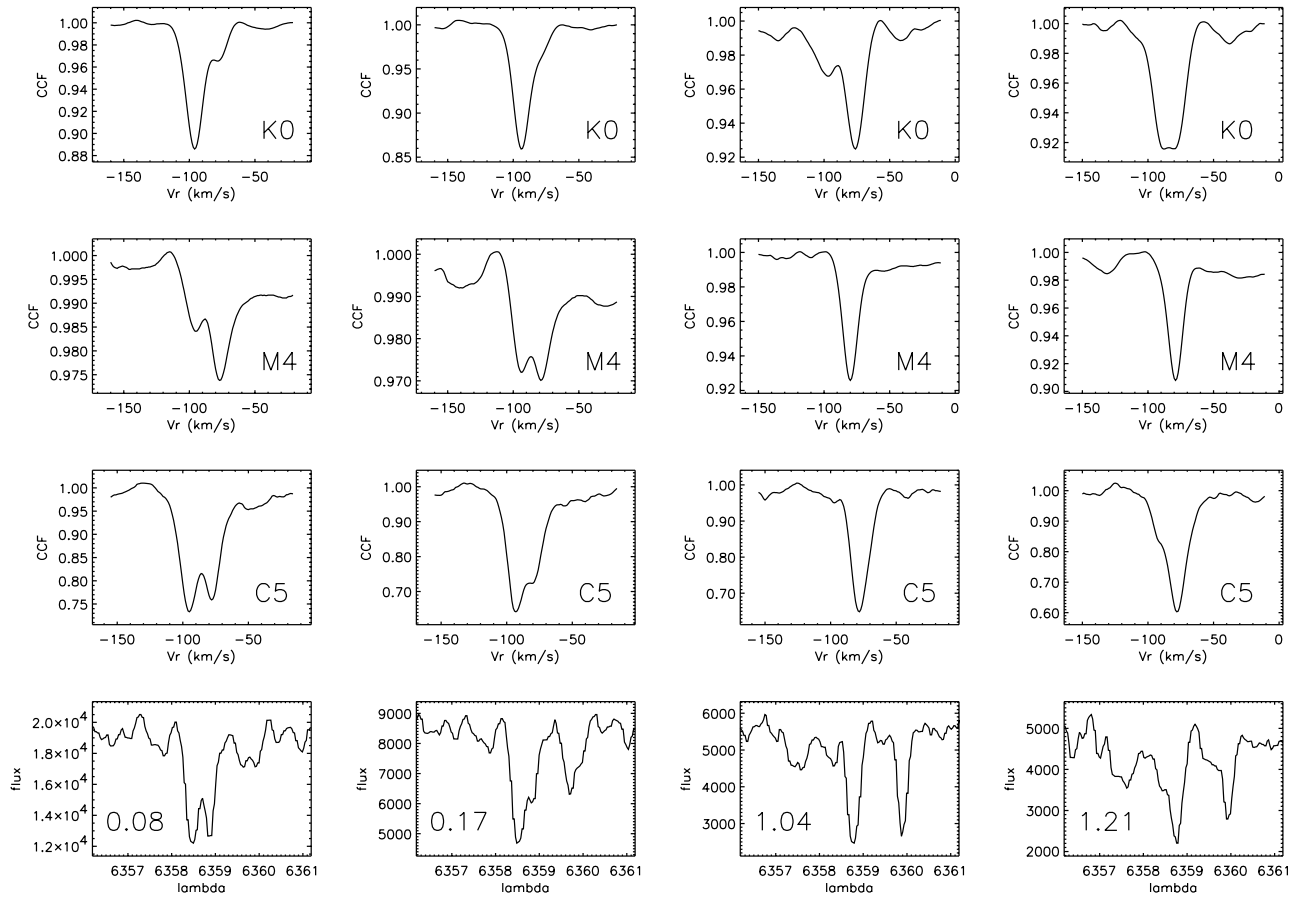

Fig. 21. Comparison of the λ 6358.69 Fe line as seen in the spectrum of Z Oph at phases 0.08, 0.17, 1.04 and 1.21 (bottom row) with the CCFs obtained with the K0-, M4- and C_5-templates (from top to bottom).

A number of checks validating the tomographic method have been presented: (i) the tomographic masks yield single-peaked CCFs at the same radial velocity (with a rms deviation of about 0.5 km s^{-1}) when applied to non-pulsating stars; (ii) the default K0- and M4-templates behave approximately like the C_2 and C_6–C_7 templates, respectively, of the $T_{\rm eff} = 3500$ K series; (iii) when checked on a spectrum of an early-type LPV that is not too crowded, the CCF profile correctly reproduces the complex shape of the lines belonging to the corresponding mask.

The application of the tomographic method to a sequence of spectra around maximum light makes it possible to follow the outward propagation of the shock front (this was demonstrated in Paper I for RT Cyg).

The method offers interesting perspectives for the study of the dynamics of LPV atmospheres. However, in its current state, its quantitative predictions (concerning for example the velocity of the shock front) remain rather limited, mainly because the geometrical radius associated with each mask is currently unknown. Spectro-interferometric observations would be necessary to make progress in that direction. Such measurements will probably become feasible with the new generation of interferometers that will be available in the near future.

Acknowledgements. RA benefits of a TMR "Marie Curie" Fellowship at ULB. A.J. is Research Associate from the *Fonds National de la Recherche Scientifique* (Belgium). This program would not have been possible without the generous allocation of telescope time at the *Observatoire de Haute-Provence* (operated by CNRS, France).

References

Adams, W. S. 1941, ApJ, 93, 11
Albrow, M. D., & Cottrell, P. L. 1996, MNRAS, 278, 337
Alvarez, R., & Plez, B. 1998, A&A, 330, 1109
Alvarez, R., Jorissen, A., Plez, B., Gillet, D., & Fokin, A. 2000, A&A, 362, 655, Paper I
Alvarez, R., Jorissen, A., Plez, B., et al. 2001, A&A, in press, Paper III
Baranne, A., Mayor, M., & Poncet, J. L. 1979, Vistas Astron., 23, 279
Baranne, A., Queloz, D., Mayor, M., et al. 1996, A&AS, 119, 373
Bessell, M. S., Castelli, F., & Plez, B. 1998, A&A, 333, 231
Delfosse, X., Forveille, T., Beuzit, J.-L., et al. 1999, A&A, 344, 897
Gillet, D., Maurice, E., Bouchet, P., & Ferlet, R. 1985, A&A, 148, 155
Hinkle, K. H., Scharlach, W. W. G., & Hall, D. N. B. 1984, ApJS, 56, 1
Karp, A. H. 1975, ApJ, 201, 641
Kaufer, A., Stahl, O., Wolf, R., et al. 1997, A&A, 320, 273
Kurucz, R. L., & Bell, B. 1995, Atomic Line data Kurucz CD-ROM No. 23, available at `http://cfa-www.harvard.edu/amdata/ampdata/amdata.html`
Magain, P. 1986, A&A, 163, 135
Plez, B. 1992, A&AS, 94, 527
Plez, B. 1998, A&A, 337, 495
Plez, B., Brett, J. M., & Nordlund, Å 1992, A&A, 256, 551
Plez, B., Smith, V. V., & Lambert, D. L. 1993, ApJ, 418, 812
Schwarzschild, M. 1952, Shock waves in the atmosphere of pulsating stars, in Transactions of the IAU, vol. VIII, ed. P. T. Oosterhoff (Cambridge University Press), 811
Serote-Roos, M., Boisson, C., & Joly, M. 1996, A&AS, 117, 93
Smith, V. V., & Lambert, D. L. 1990, ApJS, 72, 387